



Experimental determination of porosity and permeability changes induced by injection of CO₂ into carbonate rocks

L. Luquot^{*}, P. Gouze

Géosciences, Université de Montpellier 2, CNRS, Montpellier, France

ARTICLE INFO

Article history:

Accepted 24 March 2009

Keywords:

Geologic sequestration
Carbon dioxide
Porosity
Permeability
Carbonate dissolution

ABSTRACT

A set of four reactive flow-through experiments at temperature $T = 100\text{ °C}$ and total pressure $P = 12\text{ MPa}$ was performed in limestone reservoir samples. By using various ranging from 0.7 to 10 MPa, these experiments mimic mass transfers occurring (1) near the injection well, where the brine is almost saturated with CO₂ (i.e. $P_{\text{CO}_2} \approx P$), and (2) at increasing distances from the injection well, where the fluid displays lower values and higher divalent cation concentrations due rock dissolution along the fluid pathway. Results for $P_{\text{CO}_2} = 10\text{ MPa}$ show non-uniform dissolution features associated with transport-controlled mass transfer, while reaction-controlled uniform dissolution is observed for $P_{\text{CO}_2} = 2.5\text{ MPa}$. The experiment with $P_{\text{CO}_2} = 6\text{ MPa}$ allows investigating in detail the transition from transport- to reaction-controlled dissolution. Conversely, the experiment reproducing conditions far from the injection well ($P_{\text{CO}_2} = 0.7\text{ MPa}$), shows a decrease of porosity triggered by the precipitation of Mg-rich calcite. For all the dissolution experiments, the time-resolved porosity $\phi(t)$ can be modeled by a simple non-linear equation including parameters that characterise the dissolution regime triggered by the reactivity of the inlet fluid (measured by the Damköhler number, Da). Furthermore, all dissolution experiments display power scaling between permeability (k) and porosity (ϕ) with distinctly different scaling exponents characterising the reactivity of the fluid percolating the sample, independently from the decrease with time of the reactive surface area. It is shown also that dissolution at moderate positive values of Da seems the most efficient to increase permeability and promote a rapid spreading of the reaction front, while inducing minimal modification of the porosity in the vicinity of the CO₂ injection well. These results can be used to parameterize the k - ϕ function for modeling the earliest dissolution processes occurring in the vicinity of the reaction front.

© 2009 Elsevier B.V. All rights reserved.

1. Introduction

CO₂ sequestration in geological formations is increasingly being studied as a workable way of limiting the overload of CO₂ emissions in the atmosphere. CO₂ disposal into geological formations includes mainly deep saline aquifers and depleted oil reservoirs, which represent storage capacities estimated around 10^{13} kg and $4 \times 10^{11}\text{ kg}$, respectively (Holloway, 1997). The process consists of injecting more-or-less-pure CO₂ into the formation porosity through boreholes, following the same procedure routinely performed by the petroleum industry for enhancing oil recovery. In most cases, CO₂ is injected as a supercritical fluid (i.e. temperature and pressure higher than 31 °C and 7.4 MPa, respectively). Here we focus on carbonate-rich rocks which are widely present in sedimentary reservoirs.

Whatever the rock composition, the progressive dissolution of CO₂ in the formation water (generally initially at thermodynamic equilibrium with the rock-forming minerals) leads to a decrease in pH. As a result, the main expected process involves dissolution of carbonates

and, eventually, (alumino)silicates, depending on the kinetics of the individual reactions (see reviews in Plummer et al., 1978; Lasaga, 1981; Morse and Arvidson, 2002). Near the injection well, where disequilibrium is maximal, dissolution processes are expected to affect irreversibly the mechanical and hydrodynamic properties of the host rock. Specifically, dissolution leads to an increase in porosity and permeability as well as changes in the mineral reactive surface area. For a constant injection rate, the penetration distance of the dissolution front is a complex function of all these time- and space-resolved modifications. Conversely, the increase of cation concentration produced by carbonate dissolution can eventually supersaturate fluids with respect to carbonate minerals at the outermost front of the CO₂-rich plume. In this case, precipitation processes are expected leading to the decrease of porosity and permeability at this front.

Mass transfer induced by carbonate dissolution in presence of CO₂-enriched brine has been investigated following three approaches. First, dissolution rates of pure carbonate minerals, and their dependences to pH, CO₂ partial pressure (P_{CO_2}) and T , can be measured using free-drift rotating disc techniques. For instance, Pokrovsky et al. (2009 in this issue) measured the dissolution rate of calcite, dolomite and magnesite in aqueous solutions at acid to circumneutral pH, temperatures ranging from 25 to 150 °C and P_{CO_2} ranging from 1 to 5.5 MPa. Second, reaction

^{*} Corresponding author. Laboratoire Géosciences, Université Montpellier 2, CC MSE, 34095 Montpellier, France. Tel.: +33 467149066; fax: +33 467149088.

E-mail address: linda.luquot@msem.univ-montp2.fr (L. Luquot).

paths can be investigated by experimental alteration of (plurimineral) powdered rock or rock chips in closed reactors (e.g. Compton and Unwin, 1990; Alkattan et al., 1998; Kaszuba et al., 2003; Arvidson et al., 2003; Rosenbauer et al., 2005). Third, changes in rock properties can be investigated using percolation tests through cohesive rock samples to better mimic natural conditions. So far, the published studies concerned mainly P – T conditions below the supercritical threshold, i.e. $P < 7.4$ MPa and $T < 31$ °C (Noiriel et al., 2005, 2009-in this issue). In this case, pressurized CO_2 gas can be bubbled into the percolation fluid in a closed vessel and then the CO_2 -enriched fluid easily pumped and injected into the sample. Conversely, it is technically more difficult to perform percolation tests at high pressure (P) and temperature (T) conditions with P_{CO_2} corresponding to the saturation of the reservoir water in supercritical condition for CO_2 .

Quantifying the long-lasting presence of huge volumes of CO_2 in reservoirs for *in situ* P – T conditions requires addressing the essential issue of the alteration of the pore structure and the hydrodynamic properties of the reservoir induced by the chemical reactions. Fluid-rock mass transfer depends on several parameters, such as P_{CO_2} , cation concentrations, flow rate or pressure head at the boundaries, reactive surface areas, porosity, permeability, tortuosity, etc. The behaviour of these coupled processes is unpredictable without the help of numerical modelling. However, a key difficulty remains: the large variability of the characteristic space and time scales of the hydrodynamic and chemical processes. Specifically, fluid flow and hydrodynamic transport are controlled by large-scale characteristics of the porous media (e.g. the long-range correlation of the permeability field and the boundary conditions), whereas chemical reactions are controlled by local parameters at the fluid–mineral interface. Consequently, physics-based laws relating microscopic volume changes to macroscopic changes in permeability are only available for very simple models of homogeneous porous media (i.e. stacked spheres), with the assumption of homogeneous dissolution resulting from surface-controlled or diffusion-controlled mass transfer. Otherwise, the use of heuristic laws that simultaneously lump together and upscale all the processes relating mass transfer to hydrodynamic properties is required (Wong et al., 1984). At present, 70 years after the pioneering work of Kozeny (1927) and Carman (1937), most numerical models use power law permeability/porosity scaling to predict permeability changes triggered by fluid–rock mass transfers, considering implicitly that (i) porosity changes are homogeneously distributed independently on the fluid composition, and (ii) the processes by which porosity (ϕ) controls permeability (k) are local in space and time (t). The validity of these assumptions is a main issue for modelling highly reactive systems such as those expected during massive injection of CO_2 in sedimentary reservoirs. For instance, these assumptions contradict the observation that permeability scales with the size of observation, but also impose that $\partial \log(k)/\partial t$ scales with $\partial \log(\phi)/\partial t$ independently on k and on the chemical forcing. However, coupled flow and dissolution processes may induce the formation of highly conductive and spatially correlated flow channels, often referred to as wormholes (Fredd and Fogler, 1998). Wormholes grow because of the natural heterogeneity of the porous medium and the relatively fast dissolution of the carbonate phases under low pH conditions. Usual laws relating permeability to porosity cannot account for changes in the spatial correlation of properties such as observed in the presence of wormholes.

This study aims at providing experimental data that can be used to constrain the modelling of CO_2 injection and sequestration, and specifically the permeability/porosity scaling law. We present a set of four reactive percolation experiments carried out at pressure and temperatures typical of *in situ* conditions (here, $P = 12$ MPa and $T = 100$ °C). The first experiment is designed to quantify reactions occurring near the CO_2 injection zone, where the aquifer fluid is saturated with CO_2 . Additional experiments correspond to increasing distances from the injection point, where the fluid is expected to contain progressively less CO_2 and more divalent cations resulting from rock dissolution along the fluid pathway. The underlying idea is to obtain

experimental control-points in space and time corresponding to the transport of CO_2 in the reservoir during the injection phase, whereas a complete and continuous reproduction of these processes is clearly not feasible at the laboratory scale. The experimental protocol allows us to study the feedback between changes in porosity, permeability and rock structure induced by the dissolved rock-forming minerals due to reactive fluid percolation in the rock. The methodology combines chemical analysis of the fluid, continuous measurements of sample permeability, and pore-scale characterisation of the rock before and after each experiment using 3D X-ray micro-tomography (XMT). This experimental dataset is then used to investigate the dependence of the ϕ – k function on the disequilibrium state of the fluid.

2. Materials and methods

2.1. Experimental approach

The experiments consisted of injecting CO_2 -enriched fluid through a cylindrical sample core of 9 mm diameter (D) and 18 mm length (L). The four percolation experiments were carried out under *in situ* sequestration conditions ($T = 100$ °C and $P = 12$ MPa), using various partial pressures of CO_2 and different ion concentrations in rock-equilibrated fluids (brine) to simulate CO_2 -saturated brine transport during the injection phase (Fig. 1). Table 1 presents the composition of the different fluids used in the four flow-through experiments, D1, D2, D3 and P1. The geochemical code CHESS (van der Lee et al., 2002) was used to determine the pH of the injected CO_2 -enriched fluids for different fixed P_{CO_2} conditions and values of saturation index. The CO_2 -enriched fluid was injected at constant volumetric flow rate (Q), corresponding to $Q = 1.9 \times 10^{-8} \text{ m}^3 \text{ s}^{-1}$ for the three first experiments (D1, D2 and D3) and $Q = 1.0 \times 10^{-8} \text{ m}^3 \text{ s}^{-1}$ for the fourth experiment (P1). The flow rates chosen for flow experiments are higher than in natural groundwater systems in order to accelerate the processes in laboratory conditions. The first three experiments, D1 to D3, were performed at the same flow rate because we assumed these conditions represent processes in the vicinity of the injection well, whereas experiment P1 was performed at lower flow rate to mimic flow rate far away from the injection well.

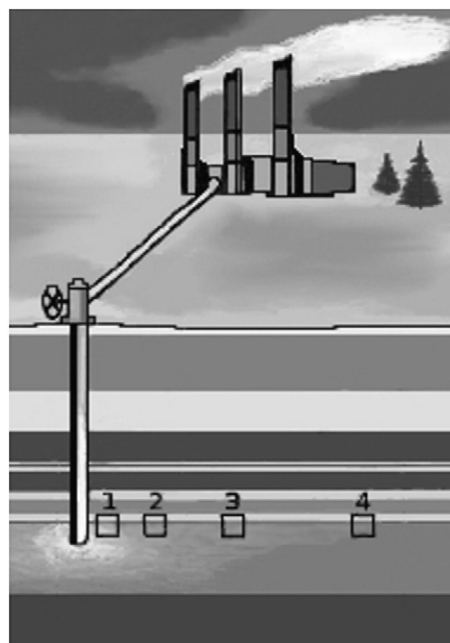


Fig. 1. Schematic illustration of a CO_2 storage facility in a sedimentary reservoir. Boxes 1 to 4 represent the decrease of CO_2 partial pressure along fluid transfer pathways into a host reservoir. For our experiments, in box 1: $P_{\text{CO}_2} = 10$ MPa (D1), box 2: $P_{\text{CO}_2} = 6$ MPa (D2), box 3: $P_{\text{CO}_2} = 2.5$ MPa (D3) and box 4: $P_{\text{CO}_2} = 0.7$ MPa (P1).

Table 1
Water composition for experiments D1, D2, D3 and P1.

Species (mmol l ⁻¹)	D1	D2	D3	P1
Na	1000	1000	1000	1000
Ca	8.25	9.37	10.0	87.5
Mg	0.16	0.19	0.21	1.85
Cl	1000	1000	1000	1000
CO ₂ (mol l ⁻¹)	0.8	0.5	0.2	0.06
P _{CO₂} (MPa)	10	6	2.5	0.75
pH	3.21	3.51	4.02	8.7
I _{out}	0.22	0.28	0.60	–
I _{in}	1.9 · 10 ⁻⁴	5.3 · 10 ⁻⁴	22.4 · 10 ⁻⁴	–

2.2. The percolation apparatus

A new experimental device (Fig. 2) was specifically engineered to mimic *in situ* massive CO₂ injection in reservoir samples at the laboratory scale for temperatures ranging from 50 to 200 °C, reservoir static pressures of 7 to 20 MPa and a partial pressure of CO₂ up to the static pressure. Resident fluids are generally moderate to high salinity brines, almost or completely equilibrated with the rock-forming minerals in the reservoir prior to the CO₂ injection. The experimental apparatus described below allows us to study systematically the processes for any combination of these parameters.

The experimental device consists in: 1) a motorized dual-piston pump system that produces the flow of reservoir brine, 2) a motorized piston pump containing liquid-phase CO₂ cooled at 5 °C, 3) the CO₂–brine mixing system, 4) the percolation cell holding the sample, and 5) the back-pressure controller/sampling system.

The two motorized piston pumps are equipped with displacement encoders, which allow an accurate control of the flow rate. This

motorized dual pump system is operated to obtain a continuous flow rate ranging from 2×10^{-9} to 2.5×10^{-8} m³ s⁻¹. The piston pump motion and the pneumatically-controlled valves are operated by a LabView-based software.

As it is difficult to control the volume ratio of a two-phase fluid mixture, i.e. liquid brine and supercritical CO₂, the mixing of the brine with CO₂ is carried out at high pressure (6 to 20 MPa) but low temperature ($T = 5$ °C). Under these conditions, CO₂ is in the liquid state, which allows to set the brine/CO₂ volume ratio corresponding to the desired CO₂ saturation of the fluid, while controlling at the same time the mixture flow rate (Fig. 3). Then, the CO₂-saturated brine is heated up to the target temperature in heated coil.

In the percolation cell, both axial and radial confining pressures are applied to the sample. To mimic natural confinement conditions, it is essential to apply a controlled confining pressure and balance the fluid injection to avoid deviatoric stresses that may damage the sample irreversibly. The axial confining pressure is applied by the axial piston, whereas the radial confining pressure is obtained by pressurization of the silicon jacket covering the sample. In the experiments, axial and radial pressures are maintained at equal values, i.e. 112% of the inlet pressure. Therefore, it can avoid damaging the rock throughout the duration of the experiment. This system is essential to minimize stresses on the sample during pressure and temperature loading and unloading, respectively at the beginning and the end of the experiment. To achieve this objective, a pressure multiplier with a free-moving piston of dissymmetric diameter is used.

The minimal pressure required to avoid degassing of the CO₂ in the circuit is controlled by a back-pressure system that imposes a constant pressure drop whatever the flow rate is. This control may become critical at low flow rates. Under such conditions, manual control is required using a micrometric valve to reduce the pressure fluctuations

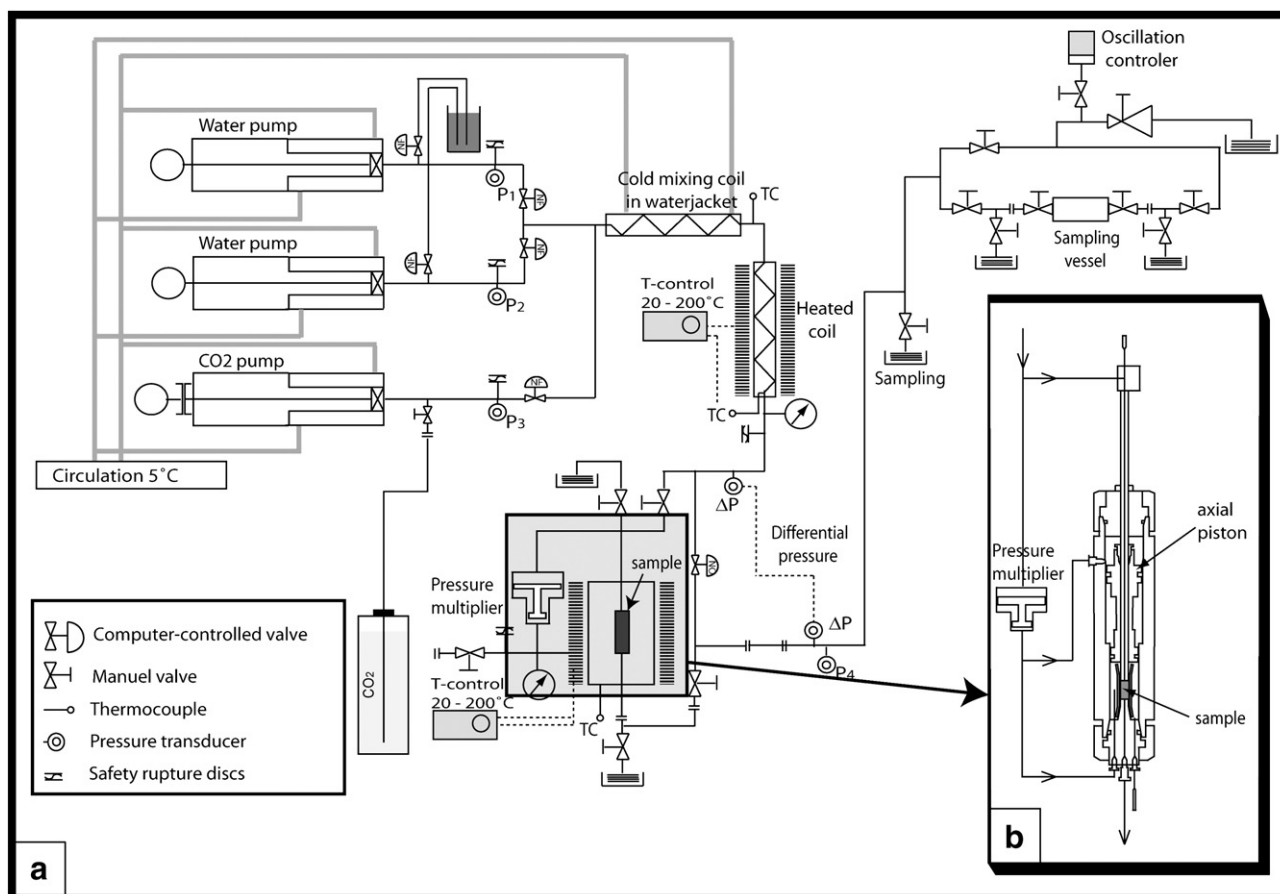


Fig. 2. a: Diagram of the experimental setup. b: Scheme of the percolation cell and the pressure multiplier.

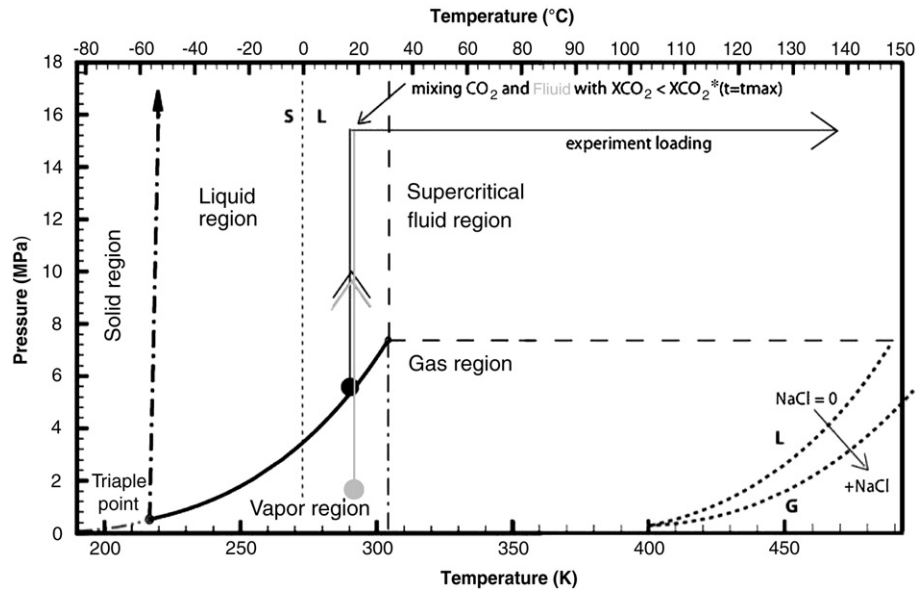


Fig. 3. P - T phase diagram for CO_2 , with P - T path corresponding to CO_2 -brine mixing.

to less than about 3%. These fluctuations have no impact on the permeability measurements because flow is steady state, storage is low and the pressure drop is measured continuously by a high-resolution differential pressure transducer.

The available flow rate enables the exploration of a wide range of hydrodynamic conditions. Specifically, this equipment allows to explore the entire range of mass transfer processes from kinetically-controlled to transport-controlled.

2.3. Sample characterisation

The samples here used in the experiment come from an oolitic limestone from the Mondeville formation of Middle Jurassic age (Paris Basin, France). The rock is essentially composed of recrystallised oolites with a mean diameter of less than a few hundred μm .

All the samples were analysed and compared by X-ray microtomography (XMT), X-ray diffraction (XRD), scanning electron microscope (SEM) and cathodoluminescence techniques, to check that samples cored alongside each other are chemically and physically similar. Sample volumes contain thousands of pores and can be regarded as a representative elementary volume (REV) of rock (de Marsily, 1981). While heterogeneities larger than the sample size are clearly not included in this REV, the experimental results can be easily upscaled to the reservoir scale in terms of matrix properties. Cathodoluminescence and SEM analyses of the four samples show no measurable differences of

the chemical or structural composition between oolites and cement composition (Fig. 4). Additional analyses on whole rocks give similar composition of the four studied samples, which corresponds to a magnesium-calcite of formula $\text{Ca}_x\text{Mg}_{1-x}\text{CO}_3$ with $\alpha = 0.99$ and $\beta = 0.01$. The initial porosity of samples calculated from post-processing the XMT images (see Noiriel et al., 2005 for the procedure) are similar in the case of 3 samples ($\phi = 7.5 \pm 0.2$) and slightly lower ($\phi = 6.8 \pm 0.1$) in the case of one sample (P1).

2.4. Monitoring changes in porosity and permeability

Sample-scale permeability $k(t)$ is calculated from the pressure difference $\Delta P(t)$ measured between the inlet and the outlet of the sample. According to Darcy's law, the ratio of the volumetric flow rate Q [$\text{m}^3 \text{s}^{-1}$] to the pressure difference ΔP [Pa] scales linearly with the sample permeability k [m^2]:

$$k(t) = -\frac{\mu L Q}{S \Delta P(t)}, \quad (1)$$

where L is the length of the sample in the flow direction [m], S is the cross-sectional area of the sample [m^2] and μ is the dynamic viscosity of the fluid [Pa s].

The fluid is collected repeatedly from the outlet port, and then analysed for Ca and Mg concentrations using Inductively Coupled

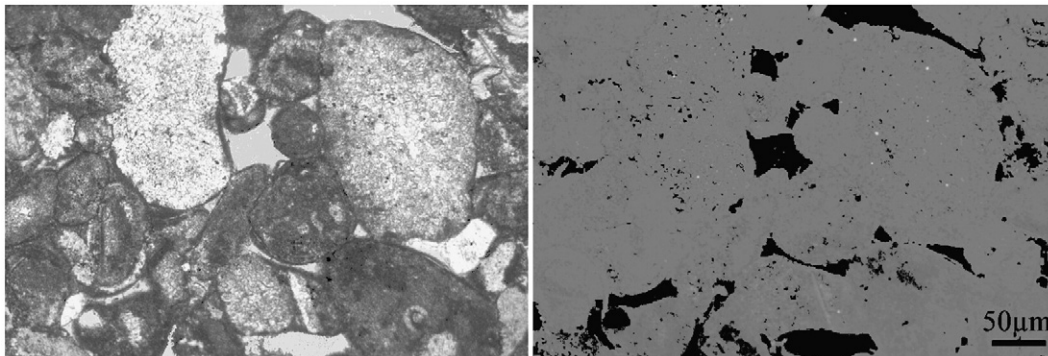


Fig. 4. Optical (left) and cathodoluminescence (right) images of a thin section taken at the edge of experiment D2 sample (before dissolution).

Plasma-Atomic Emission Spectrophotometer (ICP-AES). The volume of dissolved calcite ($V_{\text{calcite}}(t)$) is as follows:

$$V_{\text{calcite}}(t) = vQ \int_{t'=0}^t \alpha \Delta C_{\text{Ca}}(t') + \beta \Delta C_{\text{Mg}}(t') dt', \quad (2)$$

where v is the calcite molar volume ($3.7 \times 10^{-5} \text{ m}^3 \text{ mol}^{-1}$), ΔC_{Ca} and ΔC_{Mg} are the difference of calcium and magnesium concentration respectively between the outlet and the inlet fluids, and α and β are the fraction of Ca and Mg respectively in the calcite ($\alpha = 0.99$ and $\beta = 0.01$).

The sample-scale porosity $\phi(t)$ is given by:

$$\frac{\partial \phi(t)}{\partial t} = \frac{1}{V} \frac{\partial V_{\text{calcite}}(t)}{\partial t}, \quad (3)$$

where V is the total sample volume (i.e. $V = \pi L D^2 / 4$). To integrate Eq. (3), we need to know the porosity at a given time t using, for instance, the XMT images. The procedure is presented in Section 3.2.

2.5. X-ray micro-tomography

Before and after each experiment, rock samples were scanned by X-ray micro-tomography to characterise the pore-space geometry. The XMT technique is an unmatched tool for producing nondestructive three-dimensional images of rocks without any prior preparation (Flannery et al., 1987). In the present study, data acquisition was performed at the European Synchrotron Radiation Facility (ESRF) in Grenoble (France) using the ID19 beam-line. The principle of XMT is based on the 3D computed reconstruction of an object partially absorbent to X-rays, using a set of 2D radiographs acquired at different angular positions. A total of 1500 radiographs were recorded at 0.12° angle interval, using an exposure time of 2 s, thus doing a total rotation of 180° .

For each radiograph acquisition, the monochromatic X-ray beam passes through the sample and then reaches the scintillator, which converts it into visible light recorded by a high-speed digital CCD camera (2048×2048 pixels). In this study, the pixel size is $5.06 \mu\text{m}$. Synchrotron radiation provides several advantages over conventional X-ray sources, including the production of a homogeneous, parallel, monochromatic and highly coherent photon flux. This results in high-quality images having a resolution of about the size of the voxel dimension. For a given energy of the incident X-ray beam (here 40 keV), the attenuation depends on the chemical composition of the rock, specifically the atomic number of its components and their mass fraction per volume (i.e. the density). In mono-crystalline rocks such as the samples studied here, XMT images yield the distribution of densities in the rock, and allow to distinguish porosity from solid rock.

3. Results and discussion

Changes of permeability and porosity in the samples are attributed to dissolution and/or precipitation. These dynamic processes are constrained by monitoring permeability changes as well as measuring mass fluxes and sample pore structure changes. Because of the non-destructive nature of XMT imaging, the progression of the chemical reaction in the porous sample can be quantified together with the related morphological changes.

3.1. Mass transfer during reaction

Fig. 5 reports the normalized concentration $\Delta C_i(t) = C_i(t)_{\text{out}} - C_i(t)_{\text{in}}$, where i denotes the chemical species ($i = \text{Ca}$ and Mg). By convention, we define $t = 0$ as the time when the CO_2 -saturated brine starts to percolate the sample. Experiments D1, D2, D3 and P1 are set up to mimic mass transfers at locations 1, 2, 3 and 4, respectively (Fig. 1).

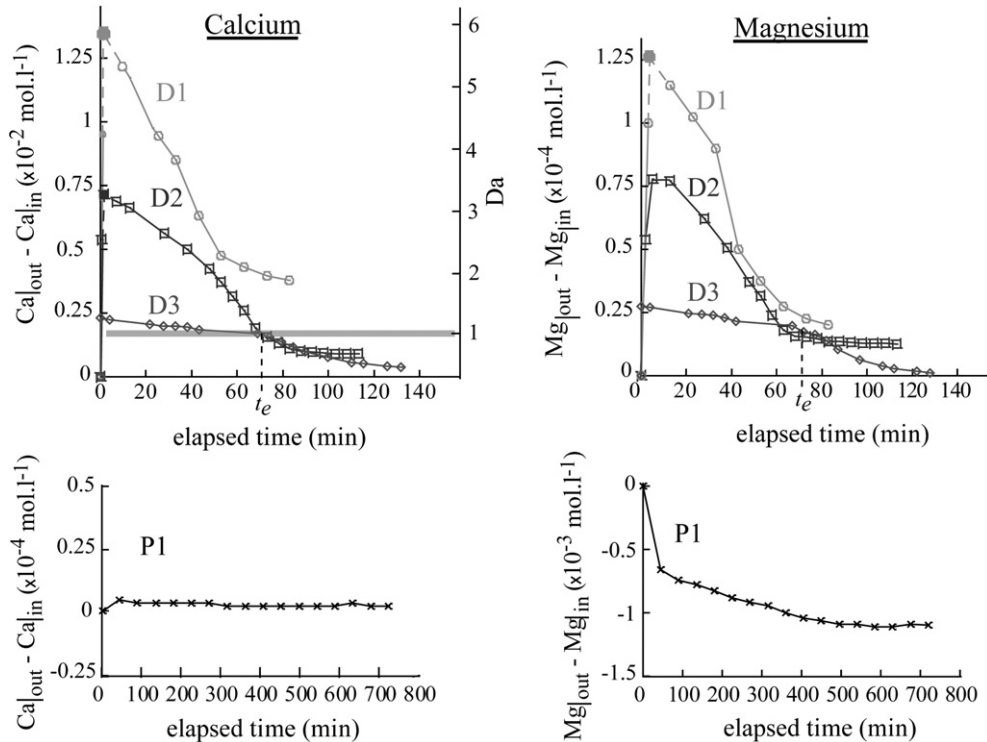


Fig. 5. Normalized time-resolved concentrations of ΔC_{Ca} and ΔC_{Mg} . Results are presented for each experiment, D1 (circles), D2 (squares), D3 (diamonds) and P1 (crosses). Note that the time scale for the dissolution experiments is not the same as for the precipitation experiment. The empty symbols denote measured concentration and the solid symbols denote the computed theoretical maximum concentration obtained accounting for the Taylor diffusion in the tubing.

3.1.1. Dissolution experiments D1, D2 and D3

The ratio $\Delta C_{\text{Ca}}(t)$ to $\Delta C_{\text{Mg}}(t)$ is roughly 99, which corresponds to the Ca/Mg mole fraction ratio of the whole rock, i.e. a magnesium-calcite of formula $\text{Ca}_{0.99}\text{Mg}_{0.01}\text{CO}_3$. $\Delta C_{\text{Ca}}(t)$ and $\Delta C_{\text{Mg}}(t)$ display similar trends indicating congruent dissolution of calcite (Fig. 5). From this point, we will describe processes using $\Delta C_{\text{Ca}}(t)$ data alone, but Ca/Mg stoichiometry of the rock-forming calcite is accounted for in the mass balance and porosity calculations (Eqs. (2) and (3)).

Experiments D1, D2 and D3 display dissolution processes, i.e. $\Delta C_{\text{Ca}}(t) > 0$. The initial increase of ΔC_{Ca} for $t < t^{(0)}$ with $t^{(0)} \approx 24$ s (i.e. $\partial \Delta C_{\text{Ca}} / \partial t > 0$) results from the Taylor dispersion of the CO_2 front in the tubes between the pump and the sample. For $t > t^{(0)}$, the breakthrough curves presented in Fig. 5 enlighten the mass transfer processes. First, as expected, the sample-scale dissolution rate is higher for the inlet fluid having the highest P_{CO_2} (experiment D1 with $P_{\text{CO}_2} = 10$ MPa). Second, sample-scale dissolution rates decrease with time (i.e. $\partial \Delta C_{\text{Ca}} / \partial t < 0$) denoting, as it will be demonstrated later (Section 3.2.), a decrease with time of the reactive surface area. Third, the rate at which the dissolution rate decreases, decreases as well ($\partial^2 \Delta C_{\text{Ca}} / \partial t^2 < 0$) in the first part of the experiments and eventually tends to zero at the end of the experiments when $\partial \Delta C_{\text{Ca}} / \partial t$ converges towards a constant value. Fourth, we observe that ΔC_{Ca} for D2 and D3 converge to a similar value for $t \geq t_e$ with $t_e \approx 70$ min, while for experiment D1 the value of ΔC_{Ca} at the end of the experiment is about five times higher. The origin of these asymptotic dissolution regimes will be discussed in Section 3.

Acknowledging that the Mg content of the rock is negligible, the dissolution reaction can be described by:



with the equilibrium constant $K_P^{T=100^\circ\text{C}} = a_{\text{Ca}^{2+}} a_{\text{HCO}_3^-} / a_{\text{H}^+} = 0.168$, where $a_i = \gamma_i C_i$ denotes the activity of species i with activity coefficient γ_i evaluated using the modified Debye–Hückel formulation for ionic strengths up to at least 2 mol.l^{-1} (Bethke, 1996). The outlet concentrations $C_{\text{Ca}}(t)_{\text{out}}$ and $C_{\text{Mg}}(t)_{\text{out}}$ are always lower than the equilibrium concentrations \bar{C}_{Ca} and \bar{C}_{Mg} , respectively, indicating that the dissolution reaction occurs far from equilibrium. Consequently, the instantaneous sample-averaged mass-transfer rate R (in $\text{mol m}^{-3} \text{ s}^{-1}$) for calcite dissolution (Eq. (4)), can be modelled using the transition state theory (Lasaga, 1998):

$$\bar{R} = \bar{r} \bar{\sigma} [1 - \bar{I}], \quad (5)$$

where \bar{r} is the kinetic rate coefficient [$\text{mol m}^{-2} \text{ s}^{-1}$] (\bar{r} is an intrinsic property of the reaction, see Pokrovsky et al., 2009-in this issue), $\bar{\sigma}$ is

the effective reaction surface area per volume of fluid [$\text{m}^2 \text{ m}^{-3}$] and \bar{I} is the saturation index:

$$\bar{I} = \frac{\text{IAP}}{K_{\text{eq}}} = \frac{a_{\text{Ca}^{2+}} a_{\text{HCO}_3^-}}{a_{\text{H}^+} K_{\text{eq}}}, \quad (6)$$

where IAP stands for the Ion Activity Product. The values of \bar{I} can be measured at the inlet and outlet of the sample only (Table 1), but the values of \bar{r} and $\bar{\sigma}$ are unknown a priori.

As described by Lasaga (1984) and then Golfier et al. (2002), the dissolution mechanism at the pore-scale can be separated into three steps: i) hydrodynamic transport of the reactants towards the surface of reaction, ii) reaction at the mineral surface, and iii) transport of reaction products away from the surface of reaction. The effective kinetic is controlled by the slowest of these three steps. It is generally accepted that transport of the solute towards and from the surface of reaction is associated with similar characteristic times. Thus, we can consider two limiting cases. If the characteristic time of reaction is short compared to the characteristic time of transport, the reaction is transport-limited. Conversely, if the hydrodynamic renewal of the reactive fluid is high, then the reaction is controlled by the mass transfer rate at the fluid–mineral interface (reaction-limited dissolution). This behaviour is characterised macroscopically by the sample-scale Damköhler number (Lasaga, 1998):

$$\text{Da}(t) = \frac{\bar{v}(t)L}{\bar{u}}(t), \quad \text{for } \text{Pe} > 1, \quad (7)$$

where \bar{v} is the sample-averaged reaction velocity [s^{-1}], L is the sample length [m], \bar{u} is the sample-averaged seepage velocity magnitude [m s^{-1}], and $\text{Pe} \equiv \bar{u}l/d_0$ denotes the sample-averaged value of the local Peclet number. The value of Pe characterises the reactant renewing at the fluid–rock interface, with d_0 the molecular diffusion ($7.5 \times 10^{-10} \text{ m}^2 \text{ s}^{-1}$ for Ca^{2+} at 25°C) and l the characteristic length of the pores [m]. Using $l \approx 0.2 \times 10^{-3} \text{ m}$ (evaluated from XMT data) and $\bar{u} = QL/\phi V \approx 3.4 \times 10^{-3} \text{ m s}^{-1}$, the values of Pe are larger than 10^2 for experiments D1 to D3, so that the Pe condition for Eq. (7) is satisfied.

If $\text{Da} < 1$, dissolution is reaction-limited, whereas dissolution is transport-limited if $\text{Da} > 1$. At the Darcy's scale, transport-limited dissolution leads to non-uniform dissolution. The localization of dissolution features is a result of positive feedback between the local increase of pore diameter and the renewal capacity of the fluid in these enlarged pores (Hoefner and Fogler, 1988; Golfier et al., 2002). In this case, the formation of highly conductive flow channels, known as

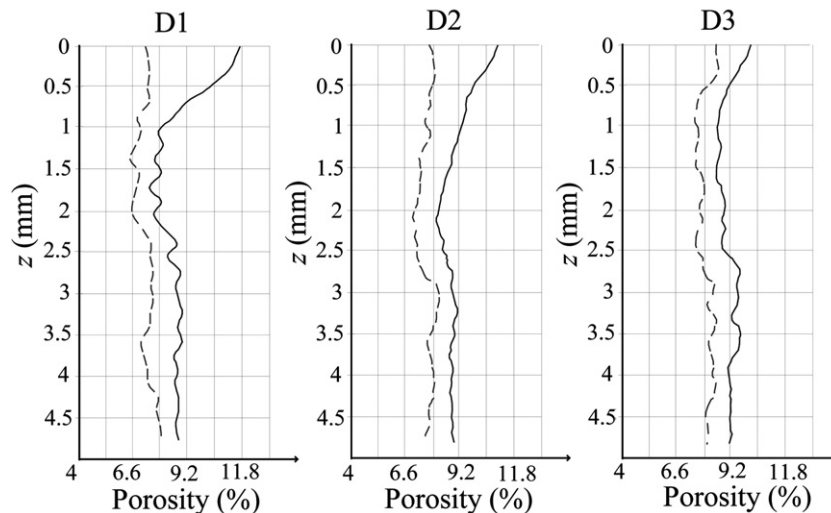


Fig. 6. x-y averaged porosity profiles along the samples in the flow direction (z) before the experiment (dotted) and after the experiment (plain).

wormholes, is expected. The distribution and shape of the wormholes are controlled by the (initial) heterogeneity of the pore structure and the correlation length of the (initial) permeability field. For the value of Pe encountered here, we expect the properties of the wormholes to be independent of Pe because the diffusive transport is negligible. While rigorously defined for reaction controlled by zero-order kinetics (i.e. rate independent of the reactant concentration), the definition of Da for the first-order kinetics law given in Eq. (5) requires introducing a concentration normalisation factor.

Using Eq. (5), the sample-averaged reaction velocity \bar{v} is:

$$\bar{v}(t) = \frac{\bar{R}(t)}{(\Delta C_{Ca})^*}, \quad (8)$$

where $(\Delta C_{Ca})^* = C_{Ca|out} - C_{Ca|in}$ is the normalization factor that is defined as the value ΔC_{Ca} for $Da = 1$. Conversely, at any time and for each of the dissolution experiments, the Ca mass balance is:

$$\Delta C_{Ca}(t) = C_{Ca}(t)|_{out} - C_{Ca}(t)|_{in} = \frac{\bar{R}(t)\bar{\phi}(t)V}{Q}. \quad (9)$$

Combining Eqs. (7)–(9), we obtain the expression of the Damköhler number as a function of the Ca concentration balance alone for a given sample length L :

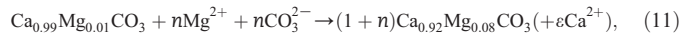
$$Da(t) = \Delta C_{Ca}(t) / (\Delta C_{Ca})^*. \quad (10)$$

According to Eq. (10), $Da \leq 1$ denotes a reaction-limited dissolution behaviour that reflects homogeneous dissolution in the sample. This is obviously the case for D3, while we observe significant wormhole structures for D1 and D2 (Figs. 6 and 7). Note however that D2 and D3 converge to a similar value of Da after 70 min ($t = t_e$). Consequently, the value of $(\Delta C_{Ca})^*$ is evidently close to the value of $C_{Ca|out} - C_{Ca|in}$ measured for D3. In the following, we assume that $(\Delta C_{Ca})^*$ is equal to $C_{Ca|out} - C_{Ca|in}$ measured for D3 and D2 at $t = t_e$; the reason for this choice will be discussed later. The expected control of the dissolution pattern by the composition of the inlet fluid is confirmed by the analysis of the XMT images (Figs. 6 and 7). For experiment D1, we observe the formation of conical penetrative wormholes associated with a large increase of porosity

localized in the vicinity of the inlet. Experiment D2 displays dissolution localisation patterns, but more diffusely distributed across and along the sample. In detail, we observe the formation of several reactive pathways described by Golfier et al. (2002) and Fredd and Fogler (1998) as ramified wormholes. In contrast, homogeneous porosity change along the sample is observed for experiment D3, with dissolution patterns that are uniformly distributed with no visible major flow paths.

3.1.2. Precipitation

For experiment P1, fluid analysis shows (Fig. 5) that $\Delta C_{Ca} > 0$ and $\Delta C_{Mg} < 0$ whatever the value of t denoting the sink of Mg within the sample, which is likely associated with Mg-enriched calcite precipitation. For $t > t^{(0)}$, $\Delta C_{Ca} \ll -\Delta C_{Mg}$ and $|\Delta C_{Ca}|$ decreases while $|\Delta C_{Mg}|$ increases with time ($|p|$ denotes the absolute value of p). This can be due to precipitation processes. SEM imaging coupled with chemical analysis indicates the occurrence of neoformed magnesium-calcite crystals of formula $Ca_\alpha Mg_\beta CO_3$ with $\alpha = 0.92 \pm 0.04$ and $\beta = 0.08 \pm 0.04$ localized at the oolite surfaces (Fig. 8). This reaction is observed in few places in the rock, mainly in some of the pore throats, and is probably controlled by local Pe and Da conditions such as described by Andreani et al. (2009). The reaction can be described by the following average formula:



where $n \approx 0.076$ is determined by a simple stoichiometric balance. Accordingly, this dissolution–precipitation process yields a volume increase of about 7.6% locally where reaction occurs and subsequently decreases the hydraulic radius of the throat and permeability decreases. These precipitation features cannot be visualized by the XMT technique, because they are smaller than the XMT resolution (i.e. 5.06 μm). At the sample scale, we observe (Fig. 10) a steady decrease in porosity for the duration of experiment ($t = 700$ min).

3.2. Porosity and specific surface changes during dissolution

As stated in Section 2.4, a reference value of the porosity is required to calculate the porosity by integration of Eq. (3). Porosity measured by processing the XMT data is expected to be misevaluated because of

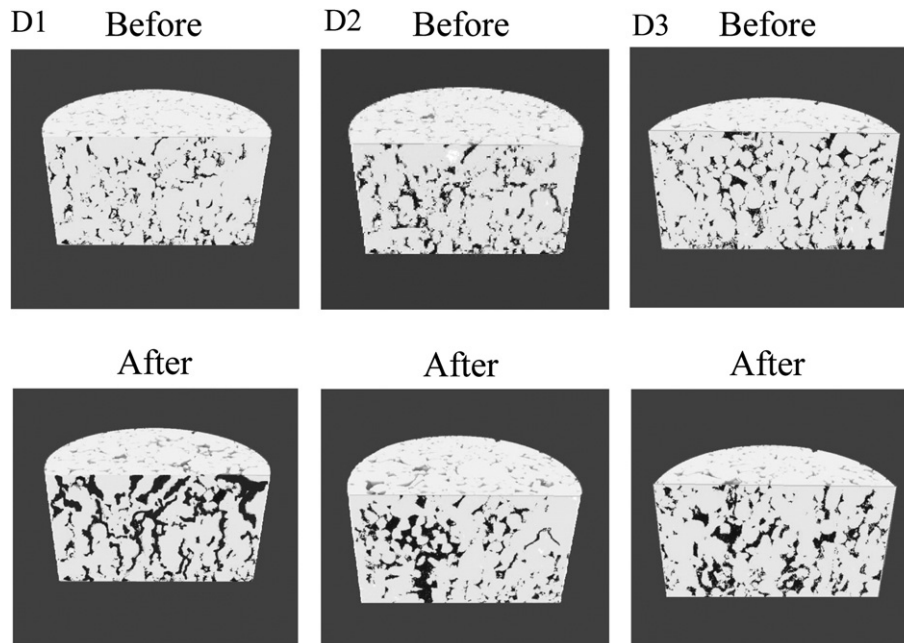


Fig. 7. 3D XMT images of the inlet side (diameter 9 mm length 4.5 mm) of cores before (top line) and after (bottom line) experiments D1, D2 and D3. Black and grey areas represent voids and solids, respectively.

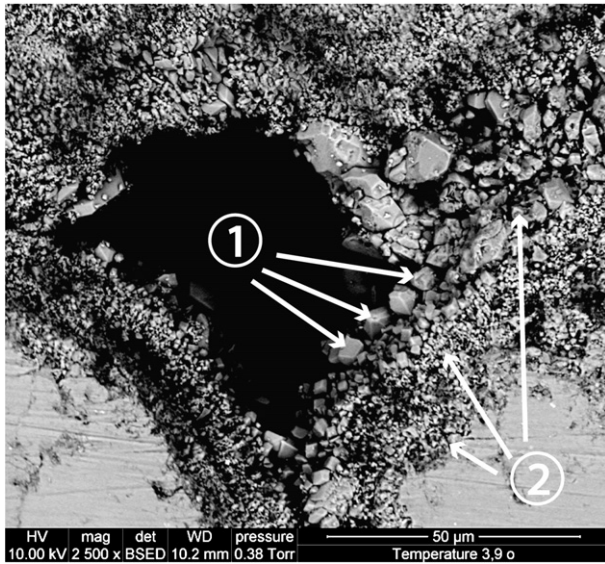


Fig. 8. SEM micrograph in secondary electron mode showing Mg-calcite (1) precipitated during experiment P1. The mean composition of the Mg-rich calcite is Ca: $23.31 \pm 0.41\%$; Mg: $1.48 \pm 0.34\%$ and CO_3 : $75.21 \pm 0.67\%$. Precipitated Mg-calcite is enriched in Mg compared to the initial rock-forming Mg-calcite (2) which the mean composition is Ca: $26.08 \pm 0.33\%$; Mg: $0.06 \pm 0.45\%$ and CO_3 : $73.86 \pm 0.58\%$.

the cutoff scale imposed by the voxel size. Indeed, the ooliths surface roughness and microstructures of the micritic cement are not properly resolved because they are smaller than the XMT resolution. Nevertheless, both the cement and oolith roughness microstructures display large reactive surface areas and are dissolved in the early stage of the experiments (Fig. 9). Consequently, for each of the dissolution experiments, the porosity measured by XMT at the end of the

experiment is the best evaluation of the porosity. Consequently, using Eq. (3), we can write the sample-averaged porosity for a given experiment as follows:

$$\bar{\phi}(t) = \bar{\phi}^{(f)} - \frac{(V_{\text{CaCO}_3})^{(f)} - V_{\text{CaCO}_3}(t)}{V}, \quad (12)$$

where $\bar{\phi}^{(f)}$ and $(V_{\text{CaCO}_3})^{(f)}$ are the porosity obtained by XMT and the volume of dissolved calcite at the end of the experiment $t = t^{(f)}$, respectively. In the case of experiment P1, the reference porosity is taken at $t = 0$ and Eq. (12) can then be rewritten as $\bar{\phi}(t) = \bar{\phi}^{(0)} + V_{\text{CaCO}_3}(t)/V$. Consequently, we expect a higher uncertainty on the value of the initial porosity $\bar{\phi}^{(0)}$. Fig. 10 presents the sample-averaged change in porosity for the four experiments. The sample-averaged mass-transfer rate $R(t)$ is calculated by introducing Eqs. (2) and (9) in Eq. (3). For any value of t we obtain:

$$\bar{R}(t) = \frac{1}{v\bar{\phi}(t)} \frac{\partial \bar{\phi}(t)}{\partial t}. \quad (13)$$

For $Da \leq 1$, dissolution is reaction-limited and is assumed spatially homogeneous (see Eq. (10)). In this case, the control of the chemical gradients in the sample (e.g. $\partial C_{\text{Ca}}/\partial z$) is negligible and Eq. (5) can be expressed in terms of sample-averaged values: $R(t) = \bar{r}'\bar{\sigma}(t)$, where $\bar{r}' = \bar{r}[1 - \bar{I}]$ is the average reaction rate defined by the composition of the inlet fluid (i.e. pH, P_{CO_2} and C_{Ca}) and thus independent of t , $\bar{\sigma}$ is the average reaction surface area per volume of fluid and \bar{I} is the average saturation index. For a given inlet composition, the sample-averaged reaction rate is controlled by the reactive surface area, that in turn is controlled by porosity: $R(t) = \bar{r}'\bar{\sigma}(\phi(t))$. Using the general formulation (see Noiriél et al., 2009-in this issue) $\bar{\sigma}(t) = \bar{\sigma}^*(\phi(t)/\bar{\phi}^*)^{-w}$, where $\bar{\sigma}^*$ and $\bar{\phi}^*$ are the values of the reactive surface area and of the porosity taken at the beginning of the homogeneous dissolution regime and w is a non-null

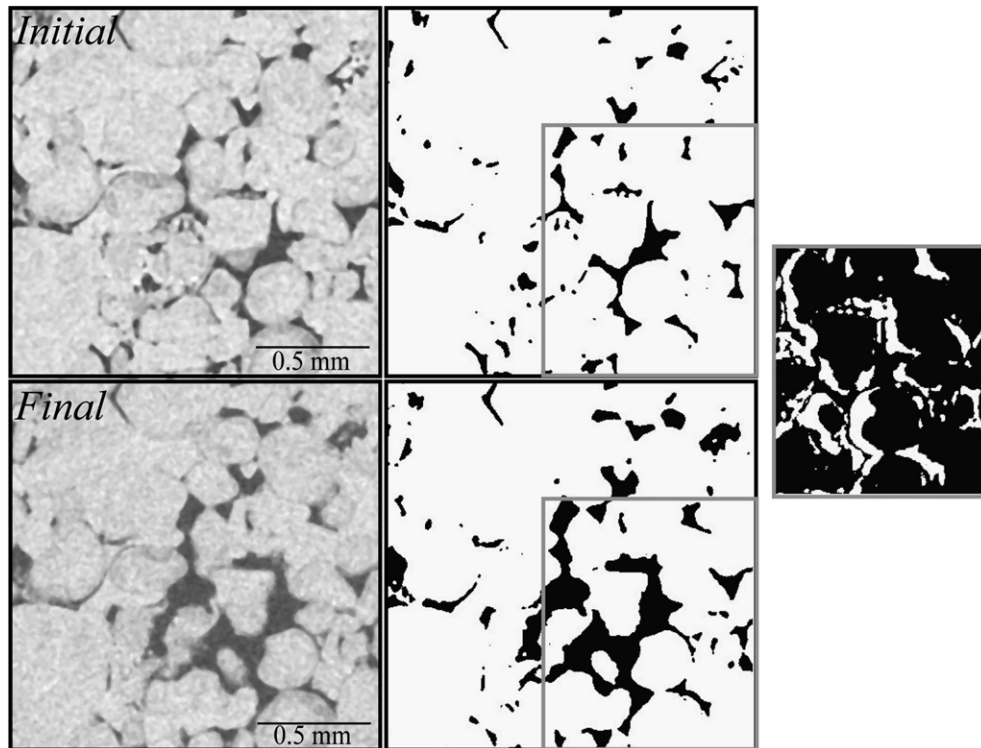


Fig. 9. XMT cross-sections of the sample used for experiment D1. Left column shows the XMT images before (top) and after (bottom) the dissolution experiment. Grey levels indicate the X-rays absorption intensity. Middle column shows the corresponding binary images, with calcite indicated in white and voids in black. The box outlined in the middle column is the area of the visualization for the right hand figure where dissolved calcite (in white) is visualized.

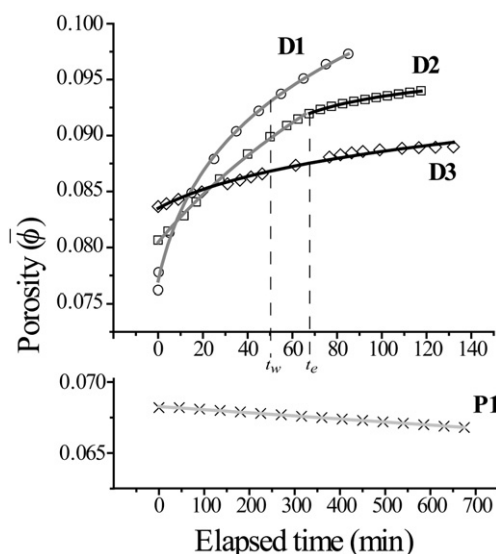


Fig. 10. Porosity calculated from Ca and Mg mass balance (Eq. (12)) for experiments D1 (circles), D2 (squares), D3 (diamonds) and P1 (crosses), and model curves (Eq. (14)).

positive coefficient, the porosity change with time is obtained by integrating Eq. (13) with respect to $\bar{\phi}$ and t . This leads to a simplified form of the non-linear Bleasdale–Nelder equation (e.g. Schabenberger and Pierce, 2001):

$$\bar{\phi}(t) = \bar{\phi}^* (1 + A(w)t)^{1/w} \quad (14)$$

with the coefficient $A(w) = \bar{r}'\bar{\sigma}^*vw$, where w and \bar{r}' characterise the reaction regime, $\bar{\phi}^*$ and $\bar{\sigma}^*$ characterise the porous media before the dissolution and v is the calcite molar volume. Accordingly, the value of $A(w)$ and w for experiments D3 ($Da \leq 1$) can be obtained by fitting the $\phi(t)$ data with Eq. (14) and $\bar{\phi}^* = \phi^{(0)}$. Experimental data and model are displayed in Fig. 10, and parameter values are given in Table 2. Interestingly, we observe also a very good fit of Eq. (14) for experiment D1 which is performed at $Da > 1$. Specifically, the entire porosity trend can be fitted with a single set of parameters (w and $A(w)$), showing that the dissolution regime is unaffected by the breakthrough of the wormholes that occurs at $t = t_w \approx 50$ min as shown by the permeability curves (see Fig. 11 and discussion below). The excellent fit of D1 data using the sample-averaged time-independent parameters \bar{r} and $[1 - \bar{I}]$ indicates that the model is pertinent for characterising non-homogeneous dissolution, or, in other words, that dissolution for $Da > 1$ can be considered as macroscopically homogeneous despite the local heterogeneity of the dissolution process. For experiment D2 one must account for the change, at $t = t_e$, from transport-limited dissolution (i.e. $Da > 1$) to reaction-rate-limited dissolution (i.e. $Da \leq 1$). Thus, two sets of parameters (w and $A(w)$) are required to fit data for $t < t_e$ and $t > t_e$ respectively, with a continuity condition for $\bar{\phi}(t = t_e)$. The excellent fit of the model, given by Eq. (14) to the porosity data for $Da > 1$, yields an important, yet unexpected,

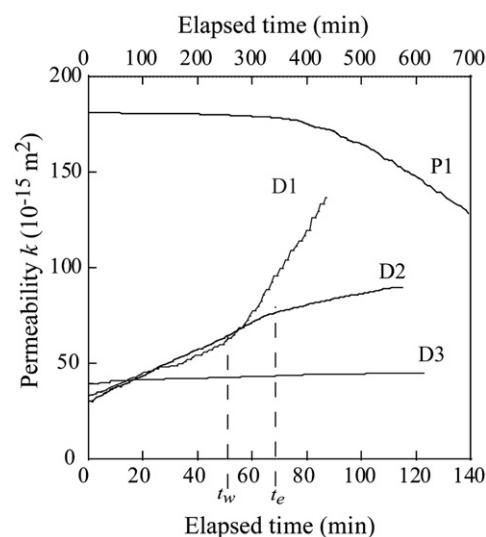


Fig. 11. Variation of sample permeability with elapsed time for the dissolution experiments (D1, D2 and D3) and the precipitation experiment P1.

conjecture: potential time-resolved mass transfer is mainly controlled by the initial dissolution regime, i.e. by the group $\bar{r}'\bar{\sigma}^*$. This term fully characterises the nominal chemical forcing within the sample, while w characterises the time-resolved efficiency of the dissolution. Fig. 12 shows that $\bar{r}'\bar{\sigma}^*$ increases with the average value of Da , i.e. with the inlet fluid disequilibrium: $(\bar{r}'\bar{\sigma}^*)_{D1} > (\bar{r}'\bar{\sigma}^*)_{D2(t < t_e)} > (\bar{r}'\bar{\sigma}^*)_{D3}$. It is worth noticing also that $(\bar{r}'\bar{\sigma}^*)_{D2(t > t_e)}$ is very similar to $(\bar{r}'\bar{\sigma}^*)_{D3}$ (see Table 2). This means that the ramified dissolution regime to homogeneous dissolution regime change (for D2) occurs for value of $\bar{r}'\bar{\sigma}^*$ that characterises $Da = 1$. Evaluating \bar{r} using the kinetic constants given by Pokrovsky et al. (2009-in this issue) and using the average value of \bar{I} calculated by the arithmetic mean between I_{in} and I_{out} (cf. Table 1), we calculate the value of $\bar{\sigma}^*$ for each of the experiments (Table 2 and Fig. 13). In opposition to what we observe for $\bar{r}'\bar{\sigma}^*$, the value of $\bar{\sigma}^*$ is inversely proportional to the average value of Da : $(\bar{\sigma}^*)_{D1} < (\bar{\sigma}^*)_{D2(t < t_e)} < (\bar{\sigma}^*)_{D3}$. This emphasizes the localization of the dissolution. The effective reactive surface area is limited when dissolution is concentrated in wormholes, while homogeneous dissolution is associated with extensive reactive

Table 2
Fitted parameters from Eq. (14) for experiments D1 to D3, and kinetics rates evaluated from Pokrovsky et al. (2009-in this issue).

	A	w	$\bar{\phi}^*$	$\bar{r}'\bar{\sigma}^*$ ($\text{mol m}^{-3} \text{ s}^{-1}$)	r' ($\times 10^{-4} \text{ mol m}^{-2} \text{ s}^{-1}$)	$\bar{\sigma}^*$ ($\times 10^6 \text{ m}^{-1}$)
D1	0.126	10.52	0.077	323.37	3.32	9.74
D2 ($t < t_e$)	0.016	5.514	0.080	80.78	0.35	23.08
D2 ($t > t_e$)	0.044	54.00	0.092	22.07	0.35	6.31
D3	0.029	23.23	0.084	34.09	0.05	68.18

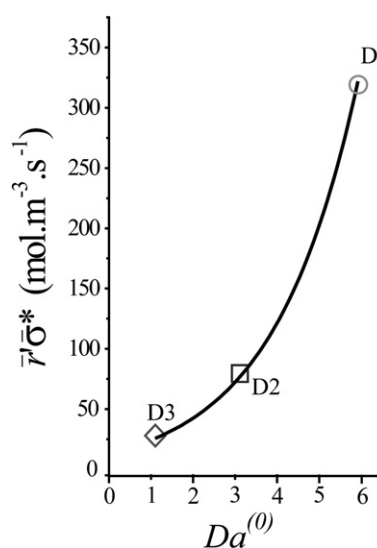


Fig. 12. $\bar{r}'\bar{\sigma}^*$ versus $Da^{(0)}$ (fitted by an exponential law) for experiment D1 (circles), D2 (squares) and D3 (diamonds).

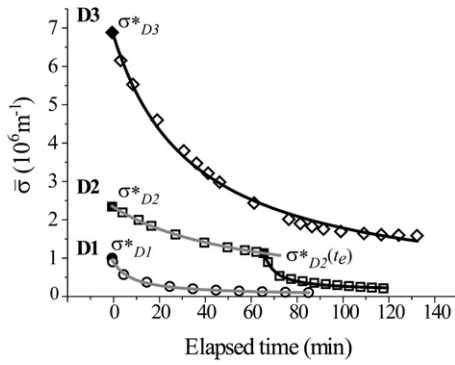


Fig. 13. Reactive specific surface $\bar{\sigma}$ versus elapsed time for experiments D1 (circles), D2 (squares) and D3 (diamonds).

surface area. Replacing $\bar{\phi}(t)$ (Eq. (14)) in Eq. (13) one can calculate the time-resolved reactive specific surface:

$$\bar{\sigma}(t) = \frac{\bar{\sigma}^*}{1 + At} \quad (15)$$

The specific surface $\bar{\sigma}(t)$ versus t for experiments D1, D2, and D3 are reported in Fig. 13. As expected $\bar{\sigma}$ decreases with time. Let us stress again that the model (Eq. (14)) used to fit the experimental porosity data (Fig. 10) and subsequently to derive the time-resolved reactive surface area (Eq. (15) and Fig. 13) is controlled by constant parameters. This emphasises that the distinctly different dissolution regimes are almost independent on the surface area changes, at least for the duration of the experiments, whereas the dissolution regime controls the change in $\bar{\sigma}(t)$ with time. This is particularly well visible in experiment D2 when at $t = t_e$ dissolution regime changes from $Da > 1$ to $Da < 1$, with a well marked change in $\partial\bar{\sigma}(t)/\partial t$.

3.3. Permeability versus porosity

The changes in permeability with time $k(t)$ for experiments D1 to D3 and P1 are reported in Fig. 11. Unsurprisingly, permeability increases in the three dissolution experiments (D1 to D3), whereas it decreases in the precipitation experiment (P1). We point out that the samples used for the three dissolution experiments are similar, with an initial permeability of $35 \pm 3 \times 10^{-15} \text{ m}^2$, while the sample used in experiment P1 has a higher initial permeability of $180 \times 10^{-15} \text{ m}^2$, even though all samples were taken side-by-side from the same core. Permeability changes are clearly linked to the composition of inlet disequibrated fluid. Experiment D1 displays an important change in permeability increase rate (dk/dt) corresponding to the breakthrough of the conical wormholes at $t_w \approx 50 \text{ min}$. Conversely, a small change in the permeability increase rate is observed at $t = t_e$ for experiment D2, while experiment D3 displays a steady but slow permeability increase with time. For experiment P1, $k(t)$ is characterised by two distinctly different rates, which are nevertheless associated with a single rate porosity decrease (Fig. 10). The origin of this behaviour will be discussed later.

The distinctly different porosity and permeability trends obtained in experiments D1 to D3 characterise dissolution patterns controlled by initial CO_2 partial pressure and the saturation index. Up to this point in the discussion, our results show that dissolution can display distinctly different patterns along the path followed by CO_2 -enriched fluids in the reservoir. However, we cannot use this observation to model reservoir-scale processes until both the porosity changes and the related permeability changes are parameterized according to the fluid composition.

Permeability is an intrinsic macroscopic property of the rock that results from a combination of several parameters including the geometry of the pores and throats, as well as, more importantly, the

sample-scale connectivity of the voids (Mavko and Nur, 1997; Pape et al., 1999). In spite of this complexity, the essential behaviour can often be evaluated from the porosity ϕ using power-law relationships following the Kozeny–Carman model (Kozeny, 1927; Carman, 1937; Dullien, 1992; Pape et al., 1999): $k \equiv \lambda \bar{\phi}^g / \tau \bar{s}^j$, where \bar{s} is the average specific surface-area, τ is the tortuosity ($\tau \geq 1$), and λ is a geometric factor expressing all the other rock-specific static parameters, while g and j reflect the dynamic behaviour of the relation. For example, the values of g and j for homogeneous sandstones (e.g. Fontainebleau sandstone) are close to 3 and 2, respectively, and up to 10 for some cemented sandstone (Bernabé et al., 2003). As a rule, tortuosity change with time is difficult to measure. Moreover, in the case of rocks displaying complex pore structure and/or when dissolution displays marked localisation, the specific surface-area cannot be measured directly. Several alternative relations have been proposed to account for deviations from the Kozeny–Carman model. For instance, Bourbié et al. (1987) proposed the scaling relation $k \equiv \lambda' \bar{\phi}^m \bar{d}^2$, where \bar{d} is the average grain diameter and m a dynamic factor. However, the definition of “grains” is useless for most limestone rocks because of the large granulometric variability and marked anisotropy of the shape of the rock clusters. Furthermore, we clearly showed that only a fraction of the porous media is concerned for transport-limited dissolution (i.e. $Da > 1$), so that grain diameter is certainly not a pertinent parameter to determine Da -dependant porosity–permeability relationship, in general.

For low-porosity media, but far from the percolation threshold, it is often observed from measurements on samples that changes in permeability scale more or less with porosity, i.e. $k \sim \bar{\phi}^n$ (Bernabé et al., 1982). The relationship $k \sim \bar{\phi}^n$ (with $n = g + jw$) can be easily derived from the Kozeny–Carman model by assuming that $\bar{s} \propto \bar{\sigma}(t) \propto \bar{\phi}^{-w}$. Accounting for the occurrence of a porosity threshold value ϕ_c below which porosity is unconnected at the scale of the sample and therefore $k = 0$, the functional relationship is (e.g. Martys et al., 1994):

$$k = \theta (\phi - \phi_c)^n, \quad (16)$$

where the unit scaling and constant parameters characterising the rock and the mass transfer processes are lumped together in θ and n , respectively. A similar power-law function was successfully used by Noiriel et al. (2004) to explain time-resolved porosity and permeability data in the course of transport-limited limestone dissolution.

Fig. 14 shows the evolution of permeability versus porosity during experiment P1. Both ϕ and k decrease as a result of Mg-rich calcite precipitation in some pore (Fig. 8). The plot of $\log(\phi)$ vs. $\log(k)$ reveals two trends with a transitional behaviour for $400 < t < 600 \text{ min}$. In the

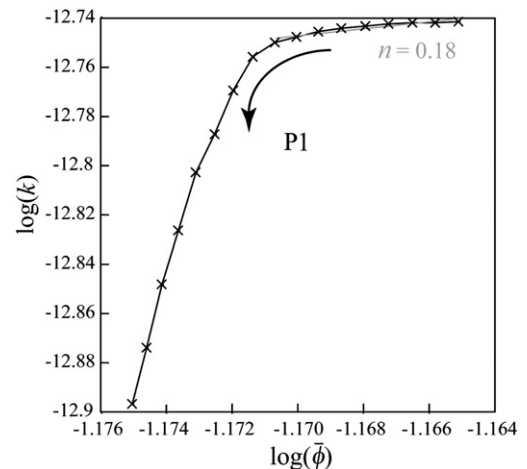


Fig. 14. Log-permeability versus log-porosity for the precipitation experiment.

first part of the experiment, the $\log(\phi)$ versus $\log(k)$ plot is linear and Eq. (16) can be applied with a very low value of the power law exponent: $n = 0.18$. For $t > 600$ min $\log(\phi)$ versus $\log(k)$ is not linear, i.e. $\partial^2(\log(k))/\partial(\log(\phi))^2 > 0$. This indicates that porosity approaches the percolation threshold ϕ_c . We use a second-order polynomial approximation to evaluate $\phi_c \approx 0.059$.

Fig. 15a displays the variation of permeability as a function of porosity during the dissolution experiments D1 to D3. For experiment D1, the variation of $\log(\phi)$ vs. $\log(k)$ displays a dual slope behaviour reflecting the wormhole breakthrough. In term of application to reservoir modelling only the first part of the curve where $n_{(D1)} = 0.79$ is useful; the second part being induced by the finite size of the sample. For experiment D2 and D3, we obtain a single-slope $\log(\phi)$ versus $\log(k)$ plot for $t > t^{(0)}$ with $n_{(D2)} = 1.24$ and $n_{(D3)} = 0.29$, respectively. This result is somewhat surprising for D2 because it implies that the change in permeability with porosity can be described as a single phenomenological process, while dissolution changes from transport-limited dissolution (i.e. $Da > 1$) to reaction-limited dissolution (i.e. $Da \leq 1$) at $t = t_c$. Fig. 15b displays n versus Da , where it can be seen that the higher value of n is obtained for experiment D2, i.e. for the experiment with intermediate value of $Da^{(0)}$ (i.e. Da for $t = t^{(0)}$). Moderate positive values of Da seems to be the most efficient to increase permeability while inducing minimal modification of the porosity in the vicinity of the injection well. Controlling the value of Da , by tuning the injection rate is certainly an effective means for keeping reservoir cohesion in the vicinity of the injection well and for promoting a rapid spreading of the reaction front. Another critical result summarized in Fig. 15b is that each of the experiment can be characterised by a single value of exponent n independently of the change with time of the sample-averaged Damköhler number (Eq. (10)) or independently of the change with time of the sample-averaged reactive surface area (Fig. 13 and Eq. (15)). For instance, results presented in Fig. 15 show that different values of n control the k – ϕ function for the same values of Da (overlapping of Da for experiments D1–D2 and D2–D3 are enlighten in Fig. 15). This result indicates that the exponent n is controlled, at least for the duration of the experiments, by the inlet fluid chemistry. This emphasizes a strong memory effect of the initial chemical forcing that controls the k – ϕ function. Yet, the short duration of the experiments does not allow determining the formulation and the characteristic time of the memory effect. Nevertheless, it can be seen from Fig. 15a that the data recorded during the last 30 min of experiment D2 seem to deviate from the main trend with lower values of the exponent n , possibly indicating a slow relaxation of the memory effect.

4. Summary and conclusions

A set of four flow-through experiments has been performed for P – T – P_{CO_2} conditions (Table 1) representative of the probable *in situ* conditions for deep saline aquifers or depleted oil reservoirs. This set of experiments has allowed us to describe mass transfer processes (1) in the vicinity of the injection well where P_{CO_2} is maximal and dissolution is non-uniform, and (2) at distant locations where dissolution becomes more and more uniform, up to a point where precipitation is observed.

As a general rule, non-uniform dissolution is expected to occur near the injection well in calcite-rich reservoirs because of the high reactivity of calcite at low pH conditions. The experiment performed with P_{CO_2} close to the total pressure P ($P_{CO_2} = 10$ MPa) shows the formation of highly conductive long-distance correlated flow channels, associate with a transport-controlled dissolution. These features strongly modify the permeability, while the macroscopic porosity is only moderately affected. For intermediate values of P_{CO_2} ($P_{CO_2} = 6$ MPa), the mass transfer changes from transport-controlled to reaction-controlled dissolution. Uniform dissolution is obtained for $P_{CO_2} = 2.5$ MPa. These three dissolution experiments display distinctly different scaling laws relating the variation of porosity versus permeability. Clearly, classical laws relating permeability to porosity using rock-dependent parameterization alone cannot account for changes in permeability triggered by local fluid–rock disequilibrium. Hence, macroscale porosity–permeability relationships must be parameterized not only to account for the rock-type-dependent properties, as generally performed when modelling low-reactive systems, but also to take account of the dissolution regime triggered by the chemical forcing.

Finally, for the experiment with $P_{CO_2} = 0.7$ MPa, i.e. reproducing conditions far from the injection well, we observe a decrease of the porosity associated with Mg–calcite precipitation in the reservoir. However, the rate of decrease in permeability rises sharply as the porosity approaches ϕ_c , indicating a probable clogging of the medium if precipitation conditions persist.

Using this set of experiments, we extract step by step the macroscopic parameters required to formulate the dependence of the porosity–permeability scaling on local fluid–rock disequilibrium:

- 1) The value of porosity at the percolation threshold is evaluated using the precipitation experiment ($P_{CO_2} = 0.7$ MPa),
- 2) The sample-scale threshold value of the Damköhler number ($Da = 1$) is defined from the uniform dissolution experiment

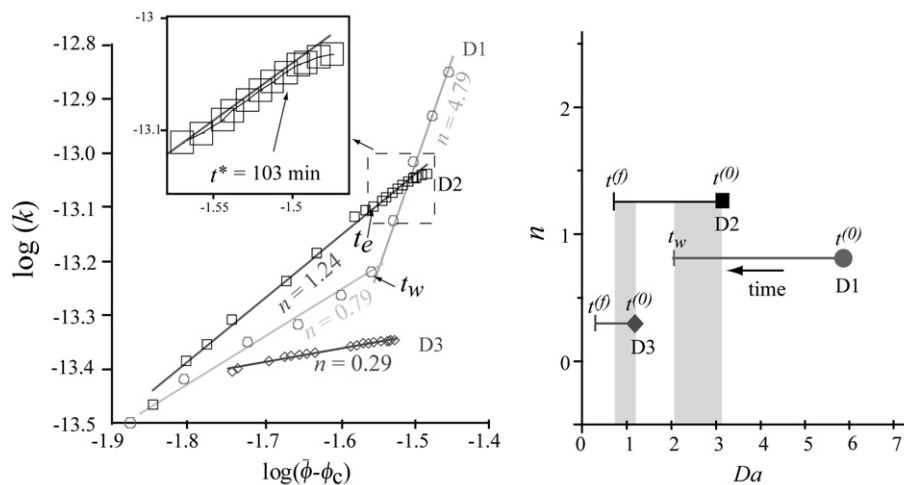


Fig. 15. a: Log-permeability versus log-porosity for the dissolution experiments D1 (circles), D2 (squares) and D3 (diamonds). Inset: Focus on the experiment D2 data for $t > t^*$, data deviate progressively from the power law model. b: Exponent n versus $Da^{(0)}$ for experiment D1 (circles), D2 (squares) and D3 (diamonds). The range of Da (t) for each of the experiment is reported (horizontal lines) as well as the overlapping between experiments D1–D2 and D2–D3.

($P_{\text{CO}_2}=2.5$ MPa), allowing us to calculate the Da number for the other experiments,

- 3) The rate of porosity increase $\partial\phi(t)/\partial t$ for each dissolution experiment is calculated from the amount of calcium released from the sample, and subsequently the time-resolved porosity is obtained using XMT images to constrain the time integration of $\partial\phi(t)/\partial t$.
- 4) The exponent n of the porosity–permeability power law $k\sim(\phi-\phi_c)^n$ is measured for dissolution and precipitation experiments.

This experimental study gives indications on the behaviours that may occur at large scale during CO_2 injection in carbonate reservoirs. At this stage of the investigation, it is impossible to parameterize ubiquitously the permeability versus porosity changes for a direct use in reservoir model. Nevertheless, the results presented here give important new indications of the challenges for modelling permeability versus porosity in highly reactive systems. Specifically, we show that the k – ϕ function at location x in the reservoir is determined by the reactivity of the fluid that first percolates this portion of the rock. Although the measured power law relationship between permeability and porosity is in agreement with several observations from measurements on samples collected in sedimentary layers and Kozeny–Carman-based model, the origin of these distinctly different power law trends in the context of dissolution, and more importantly the extrapolation of such power laws at large elapsed time is open to discussion.

Results show that both porosity changes with time and porosity–permeability power law exponent n are controlled by the inlet fluid disequilibrium and the initial effective reaction rate. Conversely, we observed that the effective reaction area and porosity, their spatial distribution as well as the structural heterogeneity that most likely controls permeability are strongly changed by dissolution, specifically for experiments with $Da>1$. Yet, the memory effect of the initial conditions and the power law increase of the permeability with porosity are not expected to last for large values of t . An evidence of this lost of memory is observed for experiment D2, where we measure a progressive deviation from the power law trend. It follows that, given an inlet fluid composition, a single parameter n allows relating permeability to porosity for $t<t^*$, where t is the elapsed time from the first arrival of the reaction front at location x and t^* is the characteristic time of the memory effect, that appears to be in the order of a few hours for highly reactive fluid in carbonates (Fig. 15). Therefore, although we believe that the parameterization of the k – ϕ function at the reaction front using the local value of the Da number may improve strongly the accuracy of the reservoir scale model, several questions arise from the results presented here. Understanding the mechanisms controlling this apparent memory effect that characterise the inertia of the feedback effect and the spatial distribution of the porosity changes on the hydrodynamic redistribution of the reactants in the sample volume require more investigations. In particular, it is essential to perform long-lasting experiments in order to explore the k – ϕ function for $t>t^*$.

Acknowledgements

This work was supported by TOTAL S.A., ADEME (Agence De l'Environnement et de la Maîtrise de l'Energie) and ANR "Captage et Stockage du CO_2 " through the project "Geocarbonate-Carbonation". These sources of funding are gratefully acknowledged. We thank John Kaszuba and the anonymous reviewer for their constructive comments.

References

- Alkattan, M., Oelkers, E.H., Dandurand, J.L., Schott, J., 1998. An experimental study of calcite and limestone dissolution rates as a function of pH from -1 to 3 and temperature from 25 to 80 °C. *Chem. Geol.* 151, 199–214.
- Andreani, M., Luquot, L., Gouze, Ph., Godard, M., Hoise, E., Gibert, B., 2009. Experimental study of carbon sequestration reactions controlled by the percolation of CO_2 -rich brine through peridotites. *Environ. Sci. Technol.* 43, 1226–1231. doi:10.1021/es8018429.
- Arvidson, R.S., Evren Ertan, I., Amonette, J.E., Luttge, A., 2003. Variation in calcite dissolution rates: a fundamental problem? *Geochim. Cosmochim. Acta* 67, 1623–1634.
- Bernabé, Y., Brace, W.F., Evans, B., 1982. Permeability, porosity and pore geometry of hot-pressed calcite. *Mech. Mater.* 1, 173–183.
- Bernabé, Y., Mok, U., Evans, B., 2003. Permeability–porosity relationships in rocks subjected to various evolution processes. *Pure Appl. Geophys.* 160 (5–6), 937–960.
- Bethke, C.M., 1996. *Geochemical Reaction Modeling*. Oxford University Press, New York. 397 pp.
- Bourbié, T., Coussy, O., Zinsner, B., 1987. *Acoustics of Porous Media*. Editions Technip, Paris. 324 pp.
- Carman, P.C., 1937. Fluid flow through granular beds. *Trans. Inst. Chem. Eng.* 15, 150–166.
- Compton, R.G., Unwin, P.R., 1990. The dissolution of calcite in aqueous solution at pH<4: kinetics and mechanism. *Philos. Trans. R. Soc. A* 330, 1–45.
- de Marsily, G., 1981. *Hydrogéologie Quantitative*. Masson, Paris. 440 pp.
- Dullien, F.A.L., 1992. *Porous Media: Fluid Transport and Pore Structure*. Academic Press, San Diego. 574 pp.
- Flannery, B., Deckman, H., Roberge, W., D'Amico, K., 1987. Three-dimensional X-ray microtomography. *Science* 237, 1439–1443.
- Fredd, C.N., Fogler, H.S., 1998. Influence of transport and reaction on wormhole formation in porous media. *AIChE J.* 44 (9), 1933–1949.
- Golfier, F., Zarcone, C., Bazin, B., Lenormand, R., Lasseux, D., Quintard, M., 2002. On the ability of a Darcy-scale model to capture wormhole formation during the dissolution of a porous medium. *J. Fluid Mech.* 457, 213–254.
- Hoefner, M.L., Fogler, H.S., 1988. Pore evolution and channel formation during flow and reaction in porous media. *AIChE J.* 34 (1), 45–54.
- Holloway, S., 1997. An overview of the underground disposal of carbon dioxide. *Energy Convers. Manag.* 38, 193–198.
- Kaszuba, J.P., Janecky, D.R., Snow, M.G., 2003. Carbon dioxide reaction processes in a model brine aquifer at 200 °C and 200 bars: implications for geologic sequestration of carbon. *Appl. Geochem.* 18 (7), 1065–1080.
- Kozeny, J., 1927. Über kapillare Leitung des Wassers im Boden. *Sitz. Akad. Wiss.* 136, 271–306.
- Lasaga, A.C., 1981. Kinetics of geochemical processes. In: Lasaga, A.C., Kirkpatrick, R.J. (Eds.), *Kinetics of Geochemical Processes. Reviews in Mineralogy*, vol. 8. Mineralogical Society of America, pp. 1–68.
- Lasaga, A.C., 1984. Chemical kinetics of water–rocks interactions. *J. Geophys. Res.* 89, 4009–4025.
- Lasaga, A.C., 1998. *Kinetic Theory in the Earth Sciences*. Princeton University Press, New Jersey. 811 p.
- Martys, N.S., Torquato, S., Bentz, P.B., 1994. Universal scaling of fluid permeability for sphere packings. *Phys. Rev. E* 50, 403–408.
- Mavko, G., Nur, A., 1997. The effect of a percolation threshold in the Kozeny–Carman relation. *Geophysics* 62 (5), 1480–1482.
- Morse, J.W., Arvidson, R.S., 2002. The dissolution kinetics of major sedimentary carbonate minerals. *Earth-Sci. Rev.* 58, 51–84.
- Noiriel, C., Gouze, Ph., Bernard, D., 2004. Investigation of porosity and permeability effects from microstructure changes during limestone dissolution. *Geophys. Res. Lett.* 31, L24603. doi:10.1029/2004GL021572.
- Noiriel, C., Bernard, D., Gouze, Ph., Thibaut, X., 2005. Hydraulic properties and microgeometry evolution in the course of limestone dissolution by CO_2 -enriched water. *Oil Gas Sci. Technol.* 60 (1), 177–192.
- Noiriel, C., Luquot, L., Madé, B., Raimbault, L., Gouze, Ph., van der Lee, J., 2009. Changes in reactive surface area during limestone dissolution: an experimental and modelling study. *Chem. Geol.* 265 (1–2), 160–170 (this issue).
- Pape, H., Clauser, C., Iffland, J., 1999. Permeability prediction based on fractal pore-space geometry. *Geophysics* 64 (5), 1447–1460.
- Plummer, L.N., Wigley, T.M.L., Parkhurst, D.L., 1978. The kinetics of calcite dissolution in CO_2 –water systems at 5 to 60 °C and 0.0 to 1.0 atm CO_2 . *Am. J. Sci.* 278, 179–216.
- Pokrovsky, O.S., Golubev, S.V., Schott, J., Castillo, A., 2009. Calcite, dolomite and magnesite dissolution kinetics in aqueous solutions at acid to circumneutral pH, 25 to 150 °C and 1 to 55 atm $p\text{CO}_2$: new constraints on CO_2 sequestration in sedimentary basins. *Chem. Geol.* 265, 20–32 (this issue).
- Rosenbauer, R.J., Koksalan, T., Palandri, J.L., 2005. Experimental investigation of CO_2 –brine–rock interactions at elevated temperature and pressure: implications for CO_2 sequestration in deep-saline aquifers. *Fuel Process. Technol.* 86, 1581–1597.
- Schabender, O., Pierce, F.J., 2001. In: Kakaç, S., Liu, H. (Eds.), *Contemporary Statistical Models for the Plant and Soil Sciences*. CRC Press. 760 pp.
- van der Lee, J., De Windt, L., Lagneau, V., Goblet, P., 2002. Presentation and application of the reactive transport code HYTEC. *Comput. Methods Water Sci.* 47, 599–606.
- Wong, P.Z., Koplik, J., Tomanic, J.P., 1984. Conductivity and permeability of rocks. *Phys. Rev. B* 30, 6606–6614.